Version of Record: https://www.sciencedirect.com/science/article/pii/S0022169421005461
Manuscript_30a0c0bb28fb9bc14f94cf80e9d1a08e

Spatial-temporal multivariate semi-Bayesian hierarchical framework for extreme precipitation frequency analysis

Álvaro Ossandón[1,a,b], Balaji Rajagopalan[a,c], William Kleiber[d]

[a] *Department of Civil, Environmental and Architectural Engineering, University of Colorado, Boulder CO*
[b] *Departamento de Obras Civiles, Universidad Técnica Santa María, Valparaíso, Chile*
[c] *CIRES, University of Colorado, Boulder CO*
[d] *Department of Applied Mathematics, University of Colorado, Boulder CO*

Abstract

We present a semi-Bayesian hierarchical modeling framework for conducting space-time frequency analysis of precipitation extremes over a large domain. In this framework, the data layer, the precipitation extreme - i.e., seasonal maximum precipitation, at each station in each year is modeled using a generalized extreme value (GEV) distribution with temporally varying parameters, which are decomposed as linear functions of covariates. The coefficients of the covariates are estimated via maximum likelihood (ML). In the process layer, the estimated ML coefficients of each of the covariates across the stations are spatially modeled with a Gaussian multivariate process which enables capturing the spatial structure and correlation between the spatial model parameters. Suitable priors are used for the spatial model hyperparameters to complete the Bayesian formulation. Since the Bayesian formulation is only at the second level, our model is semi-Bayesian and thus, the posteriors are conditional posterior distributions. With the conditional posterior

*Corresponding author: Álvaro Ossandón, alvaro.ossandon@colorado.edu

distribution of spatial fields of the GEV parameters for each time, conditional posterior distribution of the nonstationary space-time return levels of the precipitation extremes are obtained. We demonstrate this framework by application to summer precipitation extreme at 73 stations covering a large domain of Southwest US consisting of Arizona, New Mexico, Colorado, and Utah. The results from fitting and cross validation indicate that our model captures the historical variability at the stations very well. Conditional posterior distributions of return levels are simulated on a grid over the domain, which will be of immense utility in management of natural resources and infrastructure.

Keywords: Spatial extremes, Semi-Bayesian hierarchical Modeling, Nonstationary model of extremes, Southwest US summer precipitation extremes

1. Introduction

Extreme precipitation leads to extreme flow – i.e., flood events leading to loss of lives and severe damage to infrastructure. Thus, it is crucial for the engineering design of infrastructure, such as flood protection, dams, and management of water supply, and flood control to understand and model the variability of extreme precipitation in both space and time. A common practice is to perform frequency analysis on block (i.e. seasonal or annual) precipitation extreme using statistical distributions. A single set of distribution parameters are estimated assuming stationarity, in that the precipitation variability in the future will be similar to that of the past [1]. The fitted distributions are used to estimate occurrence probabilities (i.e., return period)

of rare events of desired magnitudes and return levels of desired risks – all, useful in infrastructure design [2].

Although for modeling extreme precipitation some studies have used log-normal and Gumbel distributions [3, 4], the Generalized Extreme Value (GEV) distribution, which is theoretically more appropriate, is widely used (e.g., [5, 6, 4]) due to its ability to capture a wide range of tail behaviors, and also it is consistent with extreme value theory (EVT)[2].

There are two main problems related to this single site stationary frequency analysis approach: the stationarity assumption may not be valid since diverse modeling and empirical studies have shown that the frequency and intensity of extreme climatic events are increasing and will continue to do in the foreseeable future due to climate variability and change [7, 8, 9, 10, 11]; and the need for estimating extreme precipitation at several locations where data is not available for designing of infrastructure or hazard mitigation. These motivate the need for modeling approaches that capture the variability of extremes in space and time. Temporal variability of extremes is modeled by varying the parameters of the statistical distribution as a function of covariates by a Generalized Linear Modeling [12] approach. An early approach for modeling the temporal variability of parameters of GEV as functions of time, was proposed in Katz et al. [13].

This led to plethora of studies that applied this approach at individual sites with time-varying covariates besides time trend, to modeling the temporal nonstationarity of precipitation extremes around the world. As mentioned, linear time trend to model the time-varying GEV parameters is the simplest nonstationary model [14, 15, 13]. Other time-varying covari-

ates have been used to model precipitation extremes in Asia [16, 17], North America [18, 19], Europe [20], Australia [21], and elsewhere.

Extensions of this in a Bayesian approach have been developed [22, 23, 24] which captures the uncertainties in the parameters and consequently in the return levels, robustly, via their posterior distributions. However, most of these studies are single-site analyses or assume spatial independence, thus, cannot provide estimates at any arbitrary ungauged location.

To address this, studies have extend extreme value analysis and other methods to model inter-site dependency. These include - regional frequency analysis such as the index-flood method [25]; max-stable processes [26, 27, 28, 29]; spatial modeling of marginal GEV parameters by univariate spatial Gaussian processes [30, 31, 32, 33]; capturing the spatial dependency by both Gaussian copulas and spatial modeling of marginal GEV parameters, and quantifying uncertainties of variables by hierarchical Bayesian processes of the latent parameters [34, 35]

Despite these advances, limited studies have offered models for spatial and temporal nonstationarity of climate extremes, especially precipitation extremes. Hanel et al. [36] modeled the nonstationarity in extreme precipitation over the Rhine basin using a spatial extreme value model based on the index-flow method that divided the domain into homogeneous regions where the GEV coefficients are assumed to be constant. Lima et al. [37] used a hierarchical Bayesian GEV model for flood quantile estimates in which spatial dependency is captured by scaling the GEV parameters independently according to their drainage area, i.e., independent normal prior distributions are considered for the GEV parameters. Other authors have used the same

approach to model extreme precipitation [38, 39]. Ahn et al. [40] introduced a hierarchical Bayesian model for regionalized seasonal forecasts where the spatial dependency is captured by modeling the probability distribution parameters with a multivariate Gaussian field. Bracken et al. [41] and Sun et al. [42] implemented a multivariate nonstationary Bayesian hierarchical model for hydrologic frequency analysis, in which the dependence between variables was captured by a Gaussian elliptical copula in the data layer. While these are very good approaches, some general issues remain - such as, limited ability to capture spatial dependencies over the entire domain if GEV parameters are kept constant over homogeneous regions; estimation issues with Copulas as the domain size increases; inability to capture relationships between the parameters as each parameter is modeled separately in space; these work well for smaller spatial domains or fewer variables, but become computationally intensive and have convergence issues as the domain increases, to name a few.

Our research in this paper is motivated by the need to address these issues and have the ability to obtain estimates of return levels and their uncertainties at ungauged locations. To this end, we propose a semi-Bayesian Hierarchical framework to model multi-site spatio-temporal variability of precipitation extremes.

We demonstrate this framework by its application to extreme summer precipitation at 73 stations from the Southwest US- Arizona, New Mexico, Colorado, and Utah. The paper is organized as follows. In section 2, the framework, in general, is described. The application set up for the Southwest US extreme precipitation is then described, followed by the specific form of

the model structure and fitting method in section 3. The results are described in section 4, and section 5 presents conclusions and discussion of the results.

2. Proposed framework

The proposed spatial-temporal multivariate semi-Bayesian hierarchical framework is comprised of three components: the model structure, the estimation strategy, and estimation of nonstationary return levels.

2.1. General model structure

In general, we wish to conduct a nonstationary frequency analysis of extreme precipitation at m locations over k years, and then use a spatial model that allows us to estimate return levels and their uncertainty over a grid or at stations with missing data. In this context, it is assumed that extreme precipitation series at each station follows a GEV distribution [2, 43]. The spatial dependence is captured through a spatial multivariate Gaussian process on the GEV parameters. The first layer of the hierarchical model structure, also known as the data layer, corresponds to the GEV distribution assumed at each location s_i and time point t which is

$$Y(s_i,t) \sim GEV\left(\mu(s_i,t), \sigma(s_i,t), \xi(s_i,t)\right) \quad i = 1,\ldots,m \tag{1}$$

where $\mu \in (-\infty,\infty)$ is the location parameter, $\sigma > 0$ is the scale parameter, and $\xi \in (-\infty,\infty)$ is the shape parameter. Under the nonstationary assumption, distribution parameters can vary in space and time. Thus, the three GEV parameters could be modeled as functions of time-dependent large-scale climate variables, and regional mean covariates:

$$\mu(s_i,t) = \alpha_{\mu 0}(s_i) + \sum_{j=1}^{n} \alpha_{\mu j}(s_i) Z_j(t) \quad i = 1,\ldots,m \tag{2}$$

$$\log\left(\sigma(s_i,t)\right) = \alpha_{\sigma 0}(s_i) + \sum_{j=1}^{n} \alpha_{\sigma j}(s_i) Z_j(t) \quad i = 1,\ldots,m \tag{3}$$

$$\xi(s_i,t) = \alpha_{\xi 0}(s_i) + \sum_{j=1}^{n} \alpha_{\xi j}(s_i) Z_j(t) \quad i = 1,\ldots,m \tag{4}$$

where α_μ, α_σ, and α_ξ are the regression coefficients, and $Z_j(t)$ is covariate j at the time t. $\log(\sigma)$ is modeled to ensure positive scale parameters. The regression coefficients are estimated using Maximum Likelihood (ML) approach [13]. Specific choices for covariates in our data analysis will be discussed in section 3.2.

While in many studies, ξ is modeled as a single value per study area or per region within the study area [38, 44, 45, 35], others consider that this parameter varies spatially along with the other GEV parameters, but considering a specific range of variation for it [34, 46]. Here, because we are interested in capturing the correlation between GEV parameters, no a priori restriction on its domain is imposed.

The Bayesian formulation starts in the process layer, which is the second layer of the hierarchy, assumes a multivariate spatial Gaussian process for the GEV regression coefficients obtained via ML as mentioned above. Compared to a univariate spatial Gaussian process (e.g., [31, 42]), this process can account for cross-correlation in the regression coefficients. The covariates selected for modeling the GEV parameters in the first level exhibit spatial correlation, thus, the GEV regression coefficients are likely to be correlated.

Therefore, the multivariate spatial Gaussian Process formulation is appropriate and general, regardless of the strength of the spatial correlation. Thus, the GEV regression coefficients at the location s_i are modeled as

$$\boldsymbol{\alpha}(s_i) = \boldsymbol{\beta}^T \mathbf{X}(s_i) + \mathbf{w}(s_i) + \boldsymbol{\epsilon}(s_i) \tag{5}$$

where $\boldsymbol{\alpha}(s_i) = [\boldsymbol{\alpha}_\mu(s_i), \boldsymbol{\alpha}_\sigma(s_i), \boldsymbol{\alpha}_\xi(s_i)]$ is a vector of $3(n+1) \times 1$ GEV regression coefficients at the location s_i; $\boldsymbol{\beta} = \left[\boldsymbol{\beta}_\mu, \boldsymbol{\beta}_\sigma, \boldsymbol{\beta}_\xi\right]$ is a matrix of $4 \times 3(n+1)$ spatial regression coefficients which are constant in space and time; $\mathbf{X}(s_i)$ is a 4×1 vector of regressors with the elements corresponding to the unity, coordinates, and elevation at the location s_i; and $\mathbf{w}(s_i)$ and $\boldsymbol{\epsilon}(s_i)$ are vectors of $3(n+1) \times 1$ spatial and uncorrelated residuals at location s_i, respectively. We assume the parameters can be defined through a latent multivariate process comprised of two components: a spatial term, $\mathbf{w}$, that follows a mean 0, stationary, anisotropic Gaussian process specification with a covariance function C, and independent white-noise process, $\boldsymbol{\epsilon}$.

Considering m locations, we have that spatial and uncorrelated residuals are

$$\mathbf{w} = [\mathbf{w}(s_1), \mathbf{w}(s_2), \ldots, \mathbf{w}(s_m)]^T \tag{6}$$

$$\boldsymbol{\epsilon} = [\boldsymbol{\epsilon}(s_1), \boldsymbol{\epsilon}(s_2), \ldots, \boldsymbol{\epsilon}(s_m)]^T \tag{7}$$

The spatial residuals vector, $\mathbf{w}$, follows a $MVN\,(0, \boldsymbol{\Sigma}_s)$, where $\boldsymbol{\Sigma}_s$ is the $mp \times mp$ covariance matrix and $p = 3(n+1)$. The covariance matrix is defined as

$$\boldsymbol{\Sigma}_s = \begin{bmatrix} \mathbf{C}_{11} & \cdots & \mathbf{C}_{1p} \\ \vdots & \ddots & \vdots \\ \mathbf{C}_{p1} & \cdots & \mathbf{C}_{pp} \end{bmatrix} \tag{8}$$

where $\mathbf{C}_{kl}$ is a $(m \times m)$ cross-covariance matrix. When $k = l$, it corresponds to a covariance matrix. We consider an exponential covariance function with parameters δ_{kl}^2 (the partial sill or marginal variance), ϕ_{kl} (the spatial decay parameter). The parametric form of the covariance and cross-covariance functions is

$$C_{kl}\left(s_i, s_j\right) = \delta_{kl}^2 \exp\left(-\phi_{kl}||s_i - s_j||\right) \tag{9}$$

This specification is a particular type of multivariate Matérn [47]; there are some restrictions on parameters that result in a valid, i.e., nonnegative definite covariance matrix, see Gneiting et al. [47] or Apanasovich et al. [48] for details.

For the uncorrelated residuals, we have $\boldsymbol{\epsilon} \sim MVN\left(0, \boldsymbol{\Sigma}_{ns}\right)$, where $\boldsymbol{\Sigma}_{ns}$ is $mp \times mp$ diagonal covariance matrix

$$\boldsymbol{\Sigma}_{ns} = \begin{bmatrix} \tau_1^2\mathbf{I} & 0 & \cdots & 0 \\ 0 & \tau_2^2\mathbf{I} & \cdots & 0 \\ \vdots & \vdots & \ddots & \vdots \\ 0 & 0 & \cdots & \tau_p^2\mathbf{I} \end{bmatrix} \tag{10}$$

where τ_k^2 is the nugget effect related to the kth GEV regression coefficient, and $\mathbf{I}$ is a $(m \times m)$ identity matrix.

A conceptual sketch of the spatial-temporal multivariate semi-Bayesian hierarchical framework is shown in Figure 1 which shows the data layer

(maximum likelihood estimation of the GEV regression coefficients) and the process layer (multivariate spatial Gaussian process for the GEV regression coefficients obtained in the data layer).

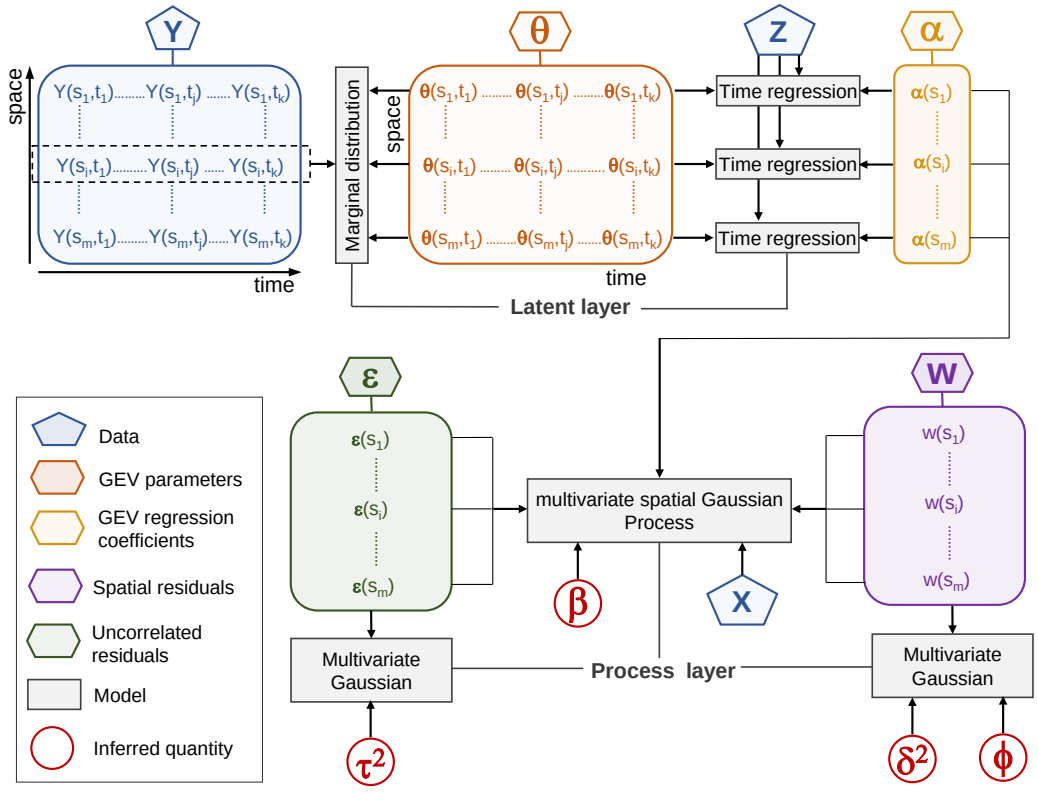

Figure 1: Conceptual sketch of the spatial-temporal multivariate semi-Bayesian hierarchical framework. $\boldsymbol{\theta}(s_i, t_j) = [\boldsymbol{\mu}(s_i, t_j), \log \boldsymbol{\sigma}(s_i, t_j), \boldsymbol{\xi}(s_i, t_j)]$.

2.2. Estimation strategy

First, GEV regression coefficients of the data layer are estimated from Equations (1)-(4) using maximum likelihood. Then, the conditional posterior distribution of the spatial regression coefficients, $\boldsymbol{\beta}$, and residuals parameters, $\boldsymbol{\delta}^2, \boldsymbol{\phi}, \boldsymbol{\tau}^2$, given maximum likelihood estimates (MLEs) of the GEV regression

coefficients, $\widehat{\boldsymbol{\alpha}}$, which are assumed as the true values of the GEV regression coefficients, and spatial regressors $\mathbf{X}$, are obtained using the multivariate Bayesian model. By Bayes' rule, the posterior distribution is

$$\begin{aligned} p\left(\boldsymbol{\beta}, \mathbf{w}, \boldsymbol{\delta}^2, \boldsymbol{\phi}, \boldsymbol{\tau}^2 | \widehat{\boldsymbol{\alpha}}, \mathbf{X}\right) &\propto p\left(\widehat{\boldsymbol{\alpha}} | \boldsymbol{\beta}, \mathbf{w}, \boldsymbol{\delta}^2, \boldsymbol{\phi}, \boldsymbol{\tau}^2, \mathbf{X}\right) \cdot p\left(\boldsymbol{\beta}, \mathbf{w}, \boldsymbol{\delta}^2, \boldsymbol{\phi}, \boldsymbol{\tau}^2 | \mathbf{X}\right) \\ &= p\left(\widehat{\boldsymbol{\alpha}} | \boldsymbol{\beta}, \mathbf{w}, \boldsymbol{\tau}^2, \mathbf{X}\right) \cdot p\left(\mathbf{w}, \boldsymbol{\delta}^2, \boldsymbol{\phi}\right) \cdot p\left(\boldsymbol{\tau}^2\right) \cdot p\left(\boldsymbol{\beta}\right) \\ &= p\left(\widehat{\boldsymbol{\alpha}} | \boldsymbol{\beta}, \mathbf{w}, \boldsymbol{\tau}^2, \mathbf{X}\right) \cdot p\left(\mathbf{w} | \boldsymbol{\delta}^2, \boldsymbol{\phi}\right) \cdot p\left(\boldsymbol{\delta}^2\right) \cdot p\left(\boldsymbol{\phi}\right) \cdot p\left(\boldsymbol{\tau}^2\right) \cdot p\left(\boldsymbol{\beta}\right) \end{aligned} \tag{11}$$

here term $p\left(\mathbf{w} | \boldsymbol{\delta}^2, \boldsymbol{\phi}\right) = f_{MVN}\left(\mathbf{w} | \mathbf{0}, \boldsymbol{\Sigma}_s\right)$; $f_{MVN}\left(\mathbf{w} | \mathbf{0}, \boldsymbol{\Sigma}_s\right)$ represents the probability density of a multivariate normal distribution with mean $\mathbf{0}$ and covariance $\boldsymbol{\Sigma}_s$ (see Equation 8); $p\left(\boldsymbol{\beta}\right) = f_{MVN}\left(\boldsymbol{\beta} | \boldsymbol{\mu}_{\boldsymbol{\beta}}, \boldsymbol{\Sigma}_{\boldsymbol{\beta}}\right)$; $\boldsymbol{\mu}_{\boldsymbol{\beta}}$ and $\boldsymbol{\Sigma}_{\boldsymbol{\beta}}$ are the spatial regression coefficient estimates and their covariance matrix obtained from a linear model fitting (Equation 5) using maximum likelihood; $p\left(\boldsymbol{\delta}^2\right)$, $p\left(\boldsymbol{\phi}\right)$, and $p\left(\boldsymbol{\tau}^2\right)$ are the priors of the other parameters, which based on Finley et al. [49] are assumed to be independent and follow the following distributions

$$\boldsymbol{\delta}^2 \sim invWishart\left(\nu, \mathbf{S}\right) \qquad \boldsymbol{\phi} \sim Unif\left(\mathbf{l}_l, \mathbf{u}_l\right) \qquad \boldsymbol{\tau}^2 \sim InvGamma\left(\boldsymbol{\kappa}, \boldsymbol{\gamma}\right) \tag{12}$$

where ν and $\mathbf{S}$ are the degrees of freedom and scale matrix of the inverse-Wishart distribution; $\boldsymbol{l}_l$ and $\boldsymbol{u}_l$ are the lower and upper limits vectors of the uniform distribution; $\boldsymbol{\kappa}$ and $\boldsymbol{\gamma}$ are the shape and scale hyper-parameters vectors of the inverse-Gamma distribution. The term $p\left(\widehat{\boldsymbol{\alpha}} | \boldsymbol{\beta}, \mathbf{w}, \boldsymbol{\tau}^2, \mathbf{X}\right)$ is the likelihood of MLEs of the GEV regression coefficients, $\widehat{\boldsymbol{\alpha}}$, conditional on the dependence of the uncorrelated residuals, the regression coefficients

$\boldsymbol{\beta} = \left[\boldsymbol{\beta}_\mu, \boldsymbol{\beta}_\sigma, \boldsymbol{\beta}_\xi\right]$, and spatial residuals. The likelihood of $\widehat{\boldsymbol{\alpha}}$ is defined as a multivariate normal

$$p\left(\widehat{\boldsymbol{\alpha}}|\boldsymbol{\beta}, \mathbf{w}, \boldsymbol{\tau}^2, \mathbf{X}\right) = f_{MVN}\left(\widehat{\boldsymbol{\alpha}}|\mathbf{X}^T\boldsymbol{\beta} + \mathbf{w}, \boldsymbol{\Sigma}_{ns}\right) \tag{13}$$

where $\mathbf{X}$ is a known $m \times p$ matrix of spatial regressors.

2.3. Nonstationary return levels

According to Read and Vogel [50], it is important to be clear when discussing nonstationary return levels and return periods since there are several definitions [51, 52, 43]. For a stationary GEV distribution the return level, T, is defined as the $p = (1 - 1/T)$th quantile

$$q_p = \mu + \frac{\sigma}{\xi}\left[(-\log p)^{-\xi} - 1\right] \tag{14}$$

Here, we use the definition for nonstationary return levels provided by Cheng et al. [51], which states that in a nonstationary setting when the GEV parameters may be time-varying, the return level can be computed at each year, which is known as the effective return level

$$q_p(t) = \mu(t) + \frac{\sigma(t)}{\xi(t)}\left[(-\log p)^{-\xi(t)} - 1\right] \tag{15}$$

3. Application

The Southwest US region comprising of the four states -Arizona, New Mexico, Colorado, and Utah- is the hottest and driest region of the United States. Most of the precipitation arrives during the winter season, but the summer precipitation makes a significant contribution to the reliability of

water resources and the health of ecology. However, summer precipitation and its extremes, over this region exhibit a high degree of spatial and temporal variability [53]. We demonstrate the utility of our proposed framework presented in the previous section by its application to summer precipitation extremes at 73 stations from this region.

3.1. Precipitation data

Daily summer, June through September, precipitation data were obtained from the Global Historical Climatology Network (GHCN)[54]. We selected stations with a full record of data for the period 1964 to 2018 or those with no more than 10% of data missing or no more than three years of missing data in a row. This resulted in 73 stations for which climatology of the extreme seasonal precipitation is shown in Figure 2 along with an elevation grid. Summer season 3-day maximum precipitation was computed for each year at each station. For a station with missing year values, these values were substituted with the median value of the station.

3.2. Covariates

Some studies [55, 56, 57] have shown that there is a weak statistical relationship between Southwest US summer precipitation and large-scale climate indices capturing drivers in tropical Pacific - El Nino Southern Oscillation (ENSO), Northern Pacific – Pacific Decadal Oscillation (PDO), and Atlantic – Atlantic Multidecadal Oscillation (AMO). Since our objective is to demonstrate our framework, we rely on these prior researches, and considered these large-scale climate indices as potential covariates, albeit with a somewhat

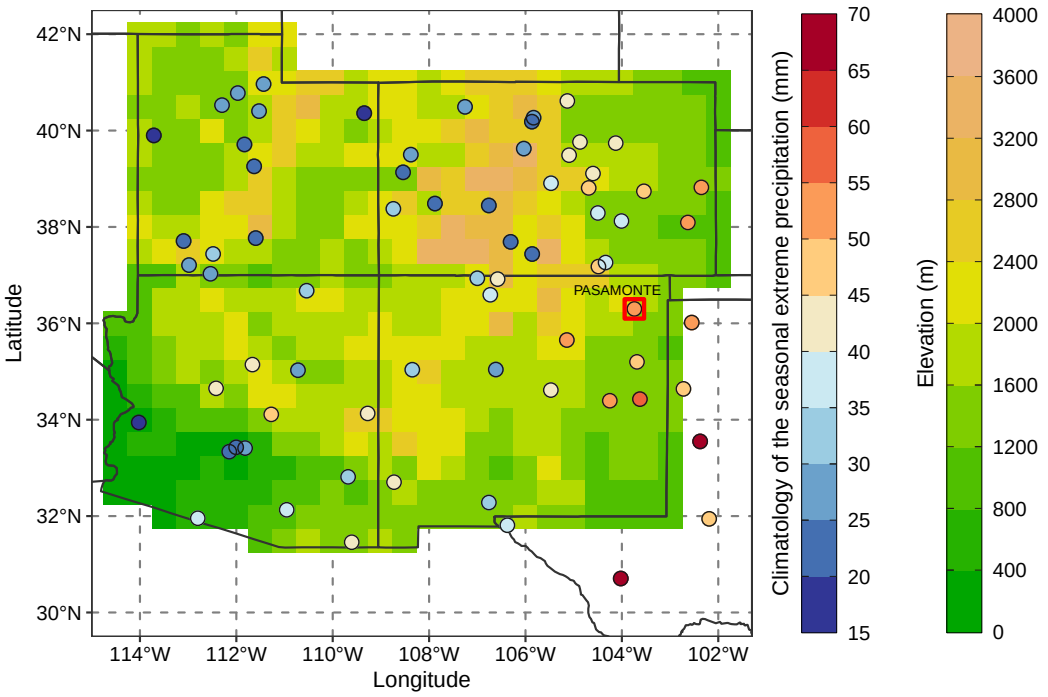

Figure 2: Climatology of the extreme seasonal precipitation for 73 precipitation stations and 0.5-degree elevation grid in (m) of the study area. The red square corresponds to the site of interest, considered in Section 4.

weaker association, for the nonstationary GEV distribution in the framework. However, users can develop tailored covariates for their specific data to enhance model performance.

For modeling the temporal nonstationarity of the GEV parameters (see Equations 2-4), first, we considered summer season average ENSO and PDO indices, and the standardized spatial average of summer seasonal precipitation (SASP) over the entire region as potential covariates. We obtained values of the multivariate ENSO index (MEI)[58, 59, 60] from `http://www.esrl.noaa.gov/psd/enso/mei/`. The PDO values [61] were obtained from

http://research.jisao.washington.edu/pdo/. The average summer season precipitation, SASP, was computed from the GHCN [54].

We assess the strength of the relationship between the covariates and the summer precipitation extreme by computing the Spearman's rank correlations, shown in Figure 3. It can be seen that SASP exhibits significant correlation with summer precipitation extreme across at almost all the locations over the domain. However, ENSO and PDO indices present a weaker correlation with precipitation extremes and significant at only few locations. Previous studies mentioned earlier in this section investigated relationship between these indices and seasonal total precipitation in this region and found them to stronger. But, from our analysis, the indices ride a weaker signature on the precipitation extremes. We selected the best nonstationary GEV model using total Akaike information criteria (AIC) [62] and total Bayesian information criterion (BIC) [63]. In this, the nonstationary model is fitted to the precipitation extreme at each location and the AIC and BIC values of all the individual location models are added to obtain the total AIC and BIC values. These are computed for a suite of candidate models with various combinations of the covariates and the model with the minimum total AIC or BIC is selected.

For modeling the GEV regression coefficients spatially, we included covariates of latitude, longitude, and elevation. Covariates were obtained at station locations and a 0.5-degree grid throughout the study area. We obtained the elevation data from the NASA Land Data Assimilation Systems (NLDAS)[64] (https://ldas.gsfc.nasa.gov/nldas/elevation).

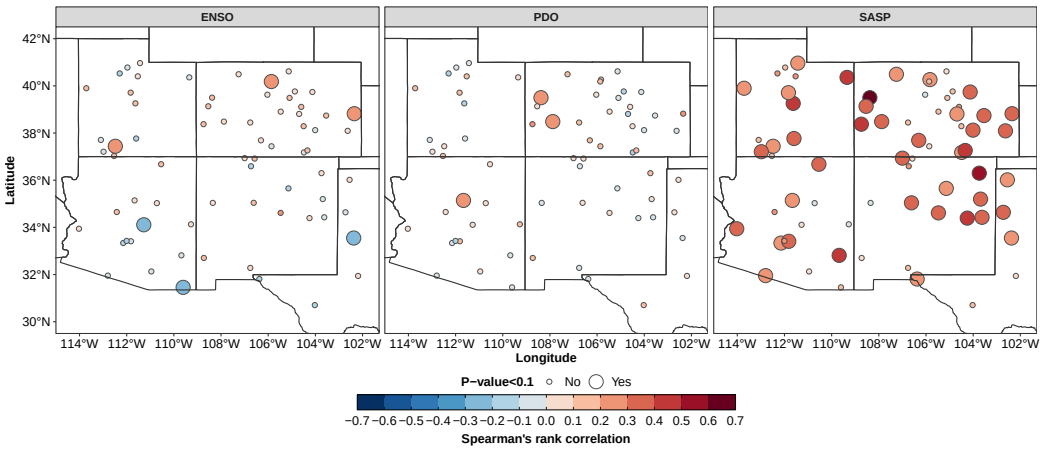

Figure 3: Spearman's rank correlation coefficient between summer 3-day maximum precipitation and covariates: (left column) ENSO; (middle column) PDO; (right column) the standardized spatial average of seasonal total precipitation. Big circles indicate that the Spearman's rank correlation is significant (P-value<0.1).

3.3. Model structure for the Southwest US

For the structure of the model for the Southwest US, we incorporated the above covariates for spatial and temporal modeling. We model the location and scale parameters of the GEV at each location, nonstationary. Shape parameters are generally more variable, leading to convergence issues in ML estimation, thus, most studies in literature generally keep this stationary. Following this, the shape parameter was keep stationary at each location. Based on both, the total AIC and BIC values, shown in Table 1, the best model selected uses only SASP as covariate to model the location and scale parameters. The next best model, though, includes ENSO. The priors on the spatial regression coefficients and residuals parameters used are:

$$\begin{aligned} \boldsymbol{\beta} &\sim MVN\left(\boldsymbol{\mu_\beta}, \boldsymbol{\Sigma_\beta}\right) \qquad \boldsymbol{\delta}^2 \sim invWishart\left(\nu, \mathbf{S}\right) \\ \boldsymbol{\phi} &\sim Unif\left(\mathbf{l}_l, \mathbf{u}_l\right) \qquad \boldsymbol{\tau}^2 \sim InvGamma\left(\boldsymbol{\kappa}, \boldsymbol{\gamma}\right) \end{aligned} \tag{16}$$

where $\boldsymbol{\beta}(s_i) = \left[\boldsymbol{\beta}_\mu, \boldsymbol{\beta}_\sigma, \boldsymbol{\beta}_\xi\right]$, $\boldsymbol{\mu_\beta}$ and $\boldsymbol{\Sigma_\beta}$ are the spatial regression coefficient estimates and their covariance matrix obtained from a linear model fitting (Equation 5) on the maximum likelihood estimates of $\boldsymbol{\alpha}$, for each GEV regression coefficient separately. Based on the recommendations from Banerjee et al. [65] and Cooley et al. [45], informative priors were were considered for the spatial residuals parameters, $\boldsymbol{\phi}$, $\boldsymbol{\delta}^2$, and noninformative priors were considered for the uncorrelated residuals parameters, $\boldsymbol{\tau}^2$. We set hyperparameter values of $\boldsymbol{\phi}$ as $\boldsymbol{l}_l = [0.2]_{6\times1}$, $\boldsymbol{u}_l = [14]_{6\times1}$, which corresponds to the range of distances for the domain considered here.

For $\boldsymbol{\delta}^2$, we set the priors based on sample variograms from the predicted residuals obtained from the linear model fitting on the maximum likelihood estimates of $\widehat{\boldsymbol{\alpha}}$, along with a exponential model which is consistent with the covariance and cross-covariance functions considered here (for more details see [66]). Sample variograms are shown in Figure 4. Thus, based on the exponential models fitted to the variograms, we considered the diagonal of the matrix $\mathbf{S}$, which is (5×5) matrix, equal to $[36, 5, 0.06, 0.05, 0.3]$ and $\nu = 6$ (number of rows of $\mathbf{S}$ plus 1). Finally, we set the hyperpameter values of $\boldsymbol{\tau}^2$ as $\boldsymbol{\kappa} = [1]_{6\times1}$ and $\boldsymbol{\gamma} = [0.01]_{6\times1}$.

Note that the priors of both spatial regression coefficients and spatial residuals are assumed to be independent. We expect the model capture the correlation in these parameters if it exists in the posterior. This would not be possible with univariate spatial Gaussian process. Since the Bayesian

Table 1: Total AIC and BIC values for different sets of covariates. for each case the same covariates are considered for location and scale parameters, and the shape parameter is considered stationary.

Covariates	AIC	BIC
ENSO	33856.7	34589.4
PDO	33858.9	34591.5
SASP	33529.0	34261.7
ENSO, PDO	33977.4	35003.2
ENSO, SASP	33657.7	34683.5
PDO, SASP	33672.4	34698.2
ENSO, PDO, SASP	33672.4	34698.2

formulation is only at the second level with the spatial model of the ML estimates, our model is semi-Bayesian and thus, the posteriors are conditional posterior distributions. With the conditional posterior distribution of spatial fields of the GEV parameters for each time, conditional posterior distribution of the nonstationary space-time return levels of the precipitation extremes are obtained.

3.4. Implementation and model fitting

The model was implemented in R using the extRemes package [67] for the data layer and the spBayes package [49] for the process layer. The parameters of the nonstationary GEV parameters at each location were estimated via maximum likelihood. The spatial Bayesian multivariate model was fit using a Markov Chain Monte Carlo (MCMC) method, specifically, Gibbs sampling

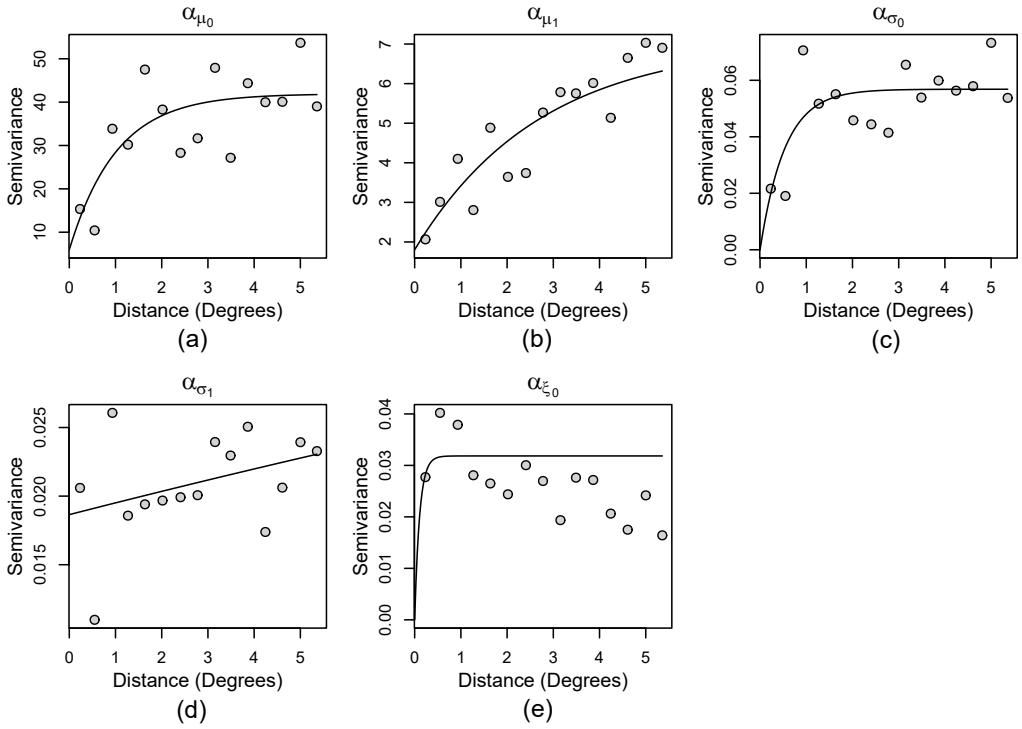

Figure 4: Sample variograms from the predicted residuals obtained from the linear model fitting on the maximum likelihood estimates of the GEV regression coefficients, $\boldsymbol{\alpha}$. Solid lines represent the least squares estimation of the exponential model of the variogram.

and random walk Metropolis steps [68]. One chain of length 120,000 was run, with the first 60,000 iterations discarded as warmup, and a sample thinning factor of 12, resulting in 5000 samples for each parameter. To assess convergence, trace plots were visually inspected, and also a Metropolis sampling acceptance percent above 80% was checked.

3.5. Computation of return levels

With the model fitted from the steps above, posterior distributions of each GEV parameter for each year are obtained at station locations or on the

0.5-degree grid by evaluating Equations (2)-(5). Thus, generated parameter values are used to compute nonstationary return levels at each station or grid point using Equation (15). The steps for this procedure are as follows:

1. Select a single conditional posterior sample of all model parameters $(\boldsymbol{\beta}, \boldsymbol{\delta}^2, \boldsymbol{\phi}, \boldsymbol{\tau}^2)$.
2. Simulate spatial and nonspatial residuals, $\mathbf{w}$ and ϵ.
3. Compute regression coefficients for GEV parameters, Equation (5).
4. Compute GEV parameters at each location i and year t, Equations (2)-(4).
5. Compute nonstationary return levels at each location i and year t, Equation (15).
6. Repeat steps 1–5 for each posterior sample.

3.6. Model comparison

To highlight the advantages of our framework, we compare it with another model. The models are as follows:

1. *Semi-Bayesian univariate*: A univariate nonstationary GEV distribution is fit to each location using MLE, where the location parameter is allowed to vary over time according to covariates specified in section 3.2. Then, the spatial dependence is captured through a spatial univariate Gaussian process on each GEV parameter.
2. *Semi-Bayesian multivariate*: The spatial-temporal semi-Bayesian multivariate hierarchical framework described in this study.

4. Results

4.1. Model fits

Figure 5 shows the Q-Q plot, the empirical Probability Density Function (PDF) and the PDF of the nonstationary GEV distribution fitted, and time series of nonstationary of the MLE return levels for different return periods for the extreme summer precipitation at Pasamonte station in New Mexico (see Figure 2). The empirical PDF in Figure 5b is obtained by a kernel density estimator which smooths the histogram (e.g., [69]). It can be seen that in general, model and sample quantiles fall close to the 1:1 line (Figure 5a), and the fitted GEV distribution captures the shape of the empirical PDF very well (Figure 5b). However, there is an overestimation of the upper tail, i.e., high values. In Figure 5c it can be seen that the nonstationary return levels capture the inter-annual variability of the observed precipitation extremes very well, in that, the return levels shift up and down in concert with the historical values. A similar or even better performance showed in Figure 5 was seen at all the other stations.

Figure 6 shows the conditional posterior median of the regression coefficients corresponding to the covariates for the location, shape, and scale parameters of GEV over the 0.5-degree grid from the 5000 simulations. The median of the intercept of the location parameter (Figure 6a) shows higher values in the eastern part of the region and lower in the western. This is consistent with the climatology of the seasonal extreme precipitation (see Figure 2) – in that the western parts are arid and semi-arid and hence lower precipitation. The conditional posterior median of SASP coefficients of the location (Figure 6b) is higher in the east, and it is positive over most of the

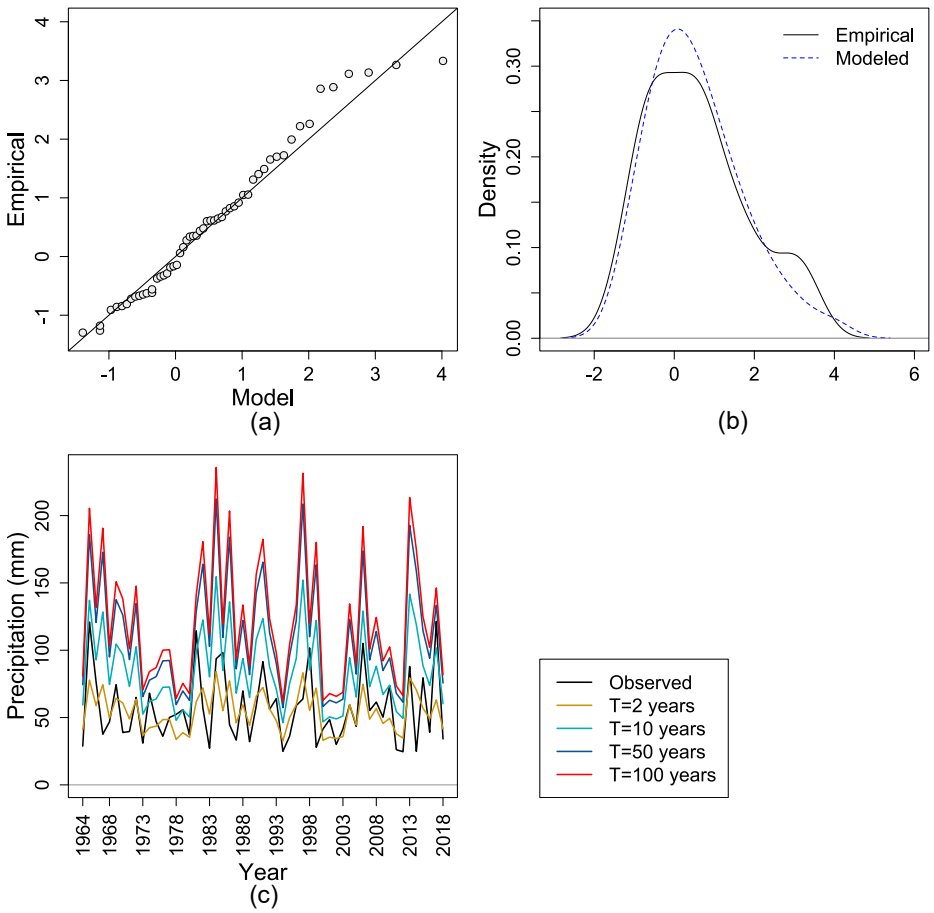

Figure 5: (a) Q-Q plot , (b) PDF of the GEV distribution fitting, and (c) time series of nonstationary of the MLE return levels for different return periods for extreme summer precipitation at Pasamonte station, NM. In panel (b), the data are first transformed to an appropriate standardized GEV scale. The empirical PDF is obtained by a kernel density estimator. In panel (c), the black line corresponds to the observed.

region with small negative regions in the middle of the domain. This can be explained by the orographic effect due to the presence of the mountain ranges. The conditional posterior median for the intercept of log of the scale parameter (Figure 6c) also shows similar spatial variability as the intercept

of the location, indicating that regions with higher extreme rainfall have higher variability. The conditional posterior median of SASP coefficients of log of the scale parameter (Figure 6d) shows similar spatial variability as the SASP coefficients of the location, i.e., higher values in the east and regions with negative values in the middle of the domain. The conditional posterior median of the shape parameter (Figure 6e) indicates heavy tail distribution (i.e. positive shape parameter) in the arid and semi-arid regions in the west part. However, its range of variation is small.

Figure 7 shows the scatter plots of the conditional posterior spatial regression coefficients β_{0,α_1} (intercept of α_1) vs. β_{0,α_0} (longitude slope of α_1) for the semi-Bayesian univariate model (Figure 7a) and semi-Bayesian multivariate model (Figure 7b). It is seen that contrary to semi-Bayesian univariate model, semi-Bayesian multivariate model can capture the cross-correlation between spatial regression coefficients for different GEV regression coefficients even when we set up uncorrelated priors for them. The same feature was observed for other spatial regression coefficients.

The same feature is observed for the residuals. This is shown in Figure 8 that displays Sample cross-variograms (for more details see [70]) of $\boldsymbol{\alpha}_{\mu_0}$-$\boldsymbol{\alpha}_{\mu_1}$ from the predicted residuals obtained from the linear model fitting on the maximum likelihood estimates (MLE) of the GEV regression coefficients (Figure 8a), the conditional posterior residuals obtained from the semi-Bayesian univariate model (Figure 8b), and the conditional posterior residuals obtained from the semi-Bayesian multivariate model (Figure 8c). Solid lines represent the least squares estimation of the exponential model of cross-variogram. It is seen that for semi-Bayesian multivariate case, poste-

rior residuals can capture the spatial cross-correlation between the residuals observed for the MLE case, the observed residuals in our case. This feature is not captured by the semi-Bayesian univariate model again. The same was observed for $\boldsymbol{\alpha}_{\mu_0}$-$\boldsymbol{\alpha}_{\sigma_0}$ and $\boldsymbol{\alpha}_{\mu_1}$-$\boldsymbol{\alpha}_{\sigma_0}$.

Thus, by capturing cross-correlation between spatial coefficients and residuals with our framework is possible to obtain more consistent simulations of the GEV regression coefficients, and consequently, reduce the uncertainty of the extreme precipitation return levels estimates.

4.2. Spatial variability of return levels

To assess the ability of the model to capture the spatial patterns of the summer precipitation extremes, we present results of 2-year return levels along with the associated observations. Figure 9 shows the spatial map of the conditional posterior median of the 2-year return level of summer precipitation extremes along with the median of the observed extremes at the station locations and also for representative wet and dry years. Figure 9a shows the conditional posterior median of the 2-year return level over all the years and the corresponding 95% credible interval width in Figure 9b. The median of historical precipitation extremes at the stations – comparable to the posterior median of the 2-year return level - are shown in Figure 9a as colored circles. It can be seen that the median values are lower in the arid and semi-arid western regions of the domain and higher in the eastern parts, which are consistent with the historical median values at the stations (the colors in the circles are consistent with that of the background from the simulations). The credible intervals widths do not show any spatial pattern. We selected a wet year (1997) in the record and show the conditional posterior median

of the 2-year return level in Figure 9c and the historical observed values at the stations are consistent with the simulations, more so in the western part of the domain. However, in the eastern part of the domain, with high precipitation, the simulations are slightly lower than the observations. The spatial pattern of the credible interval width (Figure 9d) is similar to that in Figure 9b. For a representative dry year (2001), the conditional posterior median of the 2-year return level and observed correspond very well (Figure 9e) with a similar spatial pattern of credible interval width (Figure 9f) to that of the simulations over the entire time domain (Figure 9b).

Figure 10 shows the conditional posterior median of the 100-year return level of summer precipitation extreme and its 95% confidence interval width. In Figure 10a can be seen that this, too, shows a similar spatial pattern to that of the 2-year return level, i.e., higher precipitation in the east and lower in the west. This is consistent with the spatial pattern of the intercepts of the location and log of the scale parameters (see Figure 6). As in the case of 2-year return levels, the credible intervals widths do not show any spatial pattern (Figure 10b).

4.3. Temporal variability of return levels

To assess the performance of the temporal variability of the nonstationary framework, we compared them (semi-Bayesian multivariate model) to the return levels from the MLE estimates of the GEV coefficientes, which are consider as the true values in this case, and to those return levels from the semi-Bayesian univariate model. In Figure 11 we show the boxplots of the nonstationary 100-year return level for each year at Pasamonte station, NM from the semi-Bayesian univariate model (Figure 11a) and the framework

proposed here (semi-Bayesian multivariate, Figure 11b) along with those from the MLE estimates of the GEV coefficients (red line). The whiskers show the 95% credible intervals, the boxes the interquartile range, and the horizontal lines inside the boxes, the median. The nonstationary framework proposed here shows a significant reduction in the uncertainty compared to the semi-Bayesian univariate model. This can be explained by the ability of the framework here to capture the cross-correlation between the spatial regression coefficients and between the spatial residuals (see Figures 7 and 8). So, this allow to preserve the cross-correlation at site of MLE estimates of the GEV regression coefficients for each simulation of the coefficients.

4.4. Cross-validation

To test the out-of-sample predictability of the model, cross-validation was carried out by dropping 10% of the total stations (i.e., 7 out of 73 stations), and the model was fit on the remaining 66 stations. Stations dropped are shown in Figure 12 (red circles), and were chosen to represent distinct climatological behaviors, as well as geographical sampling. To quantify the skill in a prediction mode, we made two different predictions: at the dropped stations and spatial validations. First, we predict the distributions at the dropped stations, and randomly generated 5000 samples of extreme precipitation values at the dropped locations for each year. In this case, we created boxplots for the 7 stations dropped for the validation model dropping 10% of the data (subset data model) and observed data. Next, we generated predictive posterior distributions over the 0.5-degreed grid using this model based on subset data (66 stations), and subsequently, generated 5000 samples of 100-year returns level over the same grid according to the section 3.5. We computed the difference between the median return level from the full data model (Figure 10) and this subset data model.

Figure 13 shows predicted summer precipitation extremes for the period (1964-2018) at stations dropped for the validation model dropping 10% of the data for the semi-Bayesian univariate model (light gray boxes), semi-Bayesian multivariate model (gray boxes) and the observed data (yellow boxes). The distribution from the semi-Bayesian multivariate model captures the historical distribution quite well as the box and whiskers are comparable between the two, indicating acceptable predictability, offering prospects for this approach to be used in a predictive mode. Also, it shows a better performance in capturing the historical distribution than the semi-Bayesian univariate model and a lower uncertainty. Overall, the same feature is seen for dry (2001) and wet (1997) year cases (Figure 14). Station 5 shows the worst performance, but in general, the performance is acceptable for almost all the station (yellow circles fall into the boxes).

Figure 15 shows the difference between the posterior median 100-year return levels from the full data model and the subset data model over the 0.5-degree grid. In general, the difference map does not show spatial patterns except for a bias in the south of Arizona. This bias can be caused by poor data in this region and that two of the stations dropped (stations 3 and 6) are located in this region. However, the differences are not high compared to the magnitude of 100-year return levels (Figure 10), so the performance of the model could be considered well.

5. Summary and discussion

In this study, we presented a spatial-temporal multivariate semi-Bayesian hierarchical framework for conducting nonstationary frequency analysis of precipitation extremes at ungauged locations. The framework assumes the marginal distribution of each location is a generalized extreme value (GEV) distribution, where the distribution parameters can vary in time as a function of covariates, whose coefficients are estimated via maximum likelihood. To get estimates at ungauged locations or over a grid, the spatial dependence is captured by modeling spatially the coefficients of the covariates at each station using spatial Gaussian multivariate processes.

We applied this framework to conduct nonstationary frequency analysis of extreme summer precipitation at 73 stations from the Southwest US. This application incorporated large-scale climate indexes such as ENSO and PDO and the standardized spatial average of summer seasonal precipitation (SASP) over the region as potential covariates. Based on the lowest total AIC and BIC, we selected the best model which only considers SASP as covariate for the location and scale paremeters, and stationary shape parameter. We found that the multivariate semi-Bayesian approach can capture the cross-correlation between the spatial regression coefficients and the residuals, provided a robust estimation of uncertainties of the return levels due to the spatial interpolation compared to univariate semi-Bayesian model, and capture the spatial patterns of the observed data.

In the application presented here, we only considered three potential covariates, and the shape parameter was assumed to be stationary for simplicity. However, Additional Skillful covariates can further improve the estimates

of space-time variability. In the case of that, the framework can be applied to a local scale, and local covariates can be included to capture well local patterns.

The spatial modeling of the process level parameters by incorporating correlation among the parameters makes a new contribution. Besides, this correlation enables to reduce the parameter uncertainty related to the spatial interpolation. We recognize that the uncertainty captured by our model does not represent the total uncertainty, as we are employing the Bayesian framework on the ML estimates of the GEV coefficients. The uncertainty in the ML estimates is not captured explicitly. Of course, one could include this estimation in the first layer, inside of the Bayesian framework, to capture this additional uncertainty. However, over a large spatial domain such as the Southwest U.S., this makes the model computationally intensive and with no guarantees of convergence. The semi-Bayesian model presented here, makes this tradeoff to enable an efficient model capture most of the uncertainties. A fully Bayesian framework with efficient computational methods will be a natural extension.

The model performance skill will be dependent on the strength of the temporal covariates in their association with the variability of the extremes field. In the application here, we were motivated by our ongoing research on the summer precipitation over southwest US. It is generally known that the summer precipitation and the extremes in this region exhibits high degree of variability and weaker connection with large scale forcings compared to their winter counterpart. However, the user can develop tailored covariates to their application. If the covariates are lagged in time (say a season head), this

modeling framework can be used to provide projections of seasonal extremes that will be of help in operational planning and management of natural resources ahead of the active season of extremes. Furthermore, with multi-decadal projections of the covariates, say under a global warming scenarios, projections of climate extremes for these scenarios can be made, for use by policy makers. Extensions of this framework to other fields of extremes such as streamflow, temperature, pollution concentrations in space etc., and to threshold exceedances, can be easily enabled.

Acknowledgments

This project was funded by the National Science Foundation grant 1243270. We also acknowledge the support from a Fulbright fellowship and the National Agency for Research and Development (ANID) Scholarship Program/ DOCTORADO BECAS CHILE/2015-56150013 for the first author. Partial support from the Monsoon Mission Project of the Ministry of Earth Sciences, India, for second author is thankfully acknowledged. The third author was supported by NSF DMS-1811294 and DMS-1923062. Analysis was conducted using the R language [71]. Precipitation data were downloaded from the Global Historical Climatology Network `https://www1.ncdc.noaa.gov/pub/data/ghcn/daily/`. The MEI index is downloaded from the National Oceanic and Atmospheric Administration (NOAA) Earth Systems Research Laboratory (ESRL) Physical Sciences Division `http://www.esrl.noaa.gov/psd/enso/mei/`. The PDO index is available from the University of Washington `http://research.jisao.washington.edu/pdo/`. The elevation data were downloaded from the NASA Land Data Assimilation

Systems https://ldas.gsfc.nasa.gov/nldas/elevation.

Appendix A. Abbreviations and acronyms

PDF: Probability Density Function.

GEV: Generalized extreme value.

ML: Maximum likelihood.

MLE: Maximum likelihood estimates.

AIC: Akaike information criteria.

BIC: Bayesian information criterion.

MCMC: Markov Chain Monte Carlo.

GHCN: Global Historical Climatology Network.

ENSO: El Nino Southern Oscillation.

PDO: Pacific Decadal Oscillation.

AMO: Atlantic Multidecadal Oscillation.

SASP: Standardized spatial average of summer seasonal precipitation.

MEI: Multivariate ENSO Index.

NLDAS: NASA Land Data Assimilation Systems.

References

[1] D. Jakob, Nonstationarity in extremes and engineering design, in: A. AghaKouchak, D. Easterling, K. Hsu, S. Schubert, S. Sorooshian (Eds.), Extremes in a Changing Climate, volume 65 of *Water Science and Technology Library*, Springer, Dordrecht, 2013, pp. 363–417. doi:10.1007/978-94-007-4479-0.

[2] S. Coles, An introduction to statistical modeling of extreme values, Springer, London, UK, 2001.

[3] D. M. Hershfield, Rainfall Frequency Atlas of the United States for Durations from 30 Minutes to 24 Hours and Return Periods from I to 100 Years, Technical Report, U.S. Weather Bureau, Washington, D.C., 1961.

[4] D. S. Wilks, Comparison of three-parameter probability distributions for representing annual extreme and partial duration precipitation series, Water Resources Research 29 (1993) 3543–3549. doi:10.1029/93WR01710.

[5] D. J. Dupuis, C. A. Field, Robust estimation of extremes, Canadian Journal of Statistics 26 (1998) 199–215. doi:10.2307/3315505.

[6] D. Gellens, Combining regional approach and data extension procedure for assessing GEV distribution of extreme precipitation in Belgium, Journal of Hydrology 268 (2002) 113–126. doi:10.1016/S0022-1694(02)00160-9.

[7] D. N. Barnett, S. J. Brown, J. M. Murphy, D. M. Sexton, M. J. Webb, Quantifying uncertainty in changes in extreme event frequency in response to doubled CO2 using a large ensemble of GCM simulations, Climate Dynamics 26 (2006) 489–511. doi:10.1007/s00382-005-0097-1.

[8] P. Frich, L. Alexander, P. Della-Marta, B. Gleason, M. Haylock, A. Klein Tank, T. Peterson, Observed coherent changes in climatic extremes during the second half of the twentieth century, Climate Research 19 (2002) 193–212. doi:10.3354/cr019193.

[9] IPCC, Climate change 2007: the physical science basis, Technical Report, New York, 2007.

[10] P. C. D. Milly, J. Betancourt, M. Falkenmark, R. M. Hirsch, Z. W. Kundzewicz, D. P. Lettenmaier, R. J. Stouffer, Stationarity Is Dead: Whither Water Management?, Science 319 (2008) 573 LP – 574. doi:10.1126/science.1151915.

[11] J. Schmidli, C. Frei, Trends of heavy precipitation and wet and dry spells in Switzerland during the 20th century, International Journal of Climatology 25 (2005) 753–771. doi:10.1002/joc.1179.

[12] P. McCullagh, J. A. Nelder, Generalized Linear Models, Second Edition, Taylor & Francis, 1989.

[13] R. W. Katz, M. B. Parlange, P. Naveau, Statistics of extremes in hydrology, Advances in Water Resources 25 (2002) 1287–1304. doi:10.1016/S0309-1708(02)00056-8.

[14] H. J. Fowler, D. Cooley, S. R. Sain, M. Thurston, Detecting change in UK extreme precipitation using results from the climateprediction.net BBC climate change experiment, Extremes 13 (2010) 241–267. doi:10.1007/s10687-010-0101-y.

[15] R. van Haren, G. J. van Oldenborgh, G. Lenderink, W. Hazeleger, Evaluation of modeled changes in extreme precipitation in Europe and the Rhine basin, Environmental Research Letters 8 (2013) 14053. doi:10.1088/1748-9326/8/1/014053.

[16] V. Agilan, N. V. Umamahesh, What are the best covariates for developing non-stationary rainfall Intensity-Duration-Frequency relationship?, Advances in Water Resources 101 (2017) 11–22. doi:10.1016/j.advwatres.2016.12.016.

[17] M. Gao, D. Mo, X. Wu, Nonstationary modeling of extreme precipitation in China, Atmospheric Research 182 (2016) 1–9. doi:10.1016/j.atmosres.2016.07.014.

[18] S. El Adlouni, T. B. Ouarda, X. Zhang, R. Roy, B. Bobée, Generalized maximum likelihood estimators for the nonstationary generalized extreme value model, Water Resources Research 43 (2007). doi:10.1029/2005WR004545.

[19] M. J. Um, Y. Kim, M. Markus, D. J. Wuebbles, Modeling nonstationary extreme value distributions with nonlinear functions: An application using multiple precipitation projections for U.S. cities, Journal of Hydrology 552 (2017) 396–406. doi:10.1016/j.jhydrol.2017.07.007.

[20] L. Vasiliades, P. Galiatsatou, A. Loukas, Nonstationary Frequency Analysis of Annual Maximum Rainfall Using Climate Covariates, Water Resources Management 29 (2015) 339–358. doi:10.1007/s11269-014-0761-5.

[21] V. Agilan, N. V. Umamahesh, Is the covariate based non-stationary rainfall IDF curve capable of encompassing future rainfall changes?, Journal of Hydrology 541 (2016) 1441–1455. doi:10.1016/j.jhydrol.2016.08.052.

[22] A. J. Cannon, A flexible nonlinear modelling framework for nonstationary generalized extreme value analysis in hydroclimatology, Hydrological Processes 24 (2010) 673–685. doi:10.1002/hyp.7506.

[23] L. Cheng, A. Aghakouchak, Nonstationary precipitation intensity-duration-frequency curves for infrastructure design in a changing climate, Scientific Reports 4 (2014) 1–6. doi:10.1038/srep07093.

[24] T. Ouarda, S. El-Adlouni, Bayesian nonstationary frequency analysis of hydrological variables, Journal of the American Water Resources Association 47 (2011) 496–505. doi:10.1111/j.1752-1688.2011.00544.x.

[25] H. Wazneh, F. Chebana, T. B. M. J. Ouarda, Depth-based regional index-flood model, Water Resources Research 49 (2013) 7957–7972. doi:10.1002/2013WR013523.

[26] S. G. Coles, Regional Modelling of Extreme Storms Via Max-Stable Processes, Journal of the Royal Statistical Society: Series B (Methodological) 55 (1993) 797–816. doi:10.1111/j.2517-6161.1993.tb01941.x.

[27] S. G. Coles, J. A. Tawn, Modelling Extremes of the Areal Rainfall Process, Journal of the Royal Statistical Society: Series B (Methodological) 58 (1996) 329–347. doi:10.1111/j.2517-6161.1996.tb02085.x.

[28] A. C. Davison, S. A. Padoan, M. Ribatet, Statistical modeling of spatial extremes, Statistical Science 27 (2012) 161–186. doi:10.1214/11-STS376.

[29] A. G. Stephenson, E. A. Lehmann, A. Phatak, A max-stable process model for rainfall extremes at different accumulation durations, Weather

and Climate Extremes 13 (2016) 44–53. doi:10.1016/j.wace.2016.07.002.

[30] A. V. Dyrrdal, A. Lenkoski, T. L. Thorarinsdottir, F. Stordal, Bayesian hierarchical modeling of extreme hourly precipitation in Norway, Environmetrics 26 (2015) 89–106. doi:10.1002/env.2301. arXiv:1309.6111.

[31] H. Yan, H. Moradkhani, A regional Bayesian hierarchical model for flood frequency analysis, Stochastic Environmental Research and Risk Assessment 29 (2015) 1019–1036. doi:10.1007/s00477-014-0975-3.

[32] H. Yan, H. Moradkhani, Toward more robust extreme flood prediction by Bayesian hierarchical and multimodeling, Natural Hazards 81 (2016) 203–225. doi:10.1007/s11069-015-2070-6.

[33] M. Reza Najafi, H. Moradkhani, Analysis of runoff extremes using spatial hierarchical Bayesian modeling, Water Resources Research 49 (2013) 6656–6670. doi:10.1002/wrcr.20381.

[34] C. Bracken, B. Rajagopalan, L. Cheng, W. Kleiber, S. Gangopadhyay, Spatial Bayesian hierarchical modeling of precipitation extremes over a large domain, Water Resources Research 52 (2016) 6643–6655. doi:10.1002/2016WR018768. arXiv:1512.08560.

[35] B. Renard, A Bayesian hierarchical approach to regional frequency analysis, Water Resources Research 47 (2011). doi:10.1029/2010WR010089.

[36] M. Hanel, T. A. Buishand, C. A. T. Ferro, A nonstationary index flood model for precipitation extremes in transient regional climate

694 model simulations, Journal of Geophysical Research 114 (2009) D15107.
695 doi:10.1029/2009JD011712.

696 [37] C. H. Lima, U. Lall, T. Troy, N. Devineni, A hierarchical Bayesian GEV
697 model for improving local and regional flood quantile estimates, Journal
698 of Hydrology 541 (2016) 816–823. doi:10.1016/j.jhydrol.2016.07.
699 042.

700 [38] P. Apputhurai, A. G. Stephenson, Spatiotemporal hierarchical mod-
701 elling of extreme precipitation in Western Australia using anisotropic
702 Gaussian random fields, Environmental and Ecological Statistics 20
703 (2013) 667–677. doi:10.1007/s10651-013-0240-9.

704 [39] S. Steinschneider, U. Lall, A hierarchical Bayesian regional model for
705 nonstationary precipitation extremes in Northern California conditioned
706 on tropical moisture exports, Water Resources Research 51 (2015) 1472–
707 1492. doi:10.1002/2014WR016664.

708 [40] K.-H. Ahn, R. Palmer, S. Steinschneider, A hierarchical Bayesian model
709 for regionalized seasonal forecasts: Application to low flows in the north-
710 eastern United States, Water Resources Research 53 (2017) 503–521.
711 doi:10.1002/2016WR019605.

712 [41] C. Bracken, K. D. Holman, B. Rajagopalan, H. Moradkhani, A
713 Bayesian Hierarchical Approach to Multivariate Nonstationary Hydro-
714 logic Frequency Analysis, Water Resources Research 54 (2018) 243–255.
715 doi:10.1002/2017WR020403.

[42] X. Sun, M. Thyer, B. Renard, M. Lang, A general regional frequency analysis framework for quantifying local-scale climate effects: A case study of ENSO effects on Southeast Queensland rainfall, Journal of Hydrology 512 (2014) 53–68. doi:10.1016/j.jhydrol.2014.02.025.

[43] R. W. Katz, Statistical Methods for Nonstationary Extremes, in: A. AghaKouchak, D. Easterling, K. Hsu, S. Schubert, S. Sorooshian (Eds.), Extremes in a Changing Climate, 65 ed., Springer, Dordrecht, 2013, pp. 15–37.

[44] J. Atyeo, D. Walshaw, A region-based hierarchical model for extreme rainfall over the UK, incorporating spatial dependence and temporal trend, Environmetrics 23 (2012) 509–521. doi:10.1002/env.2155.

[45] D. Cooley, D. Nychka, P. Naveau, Bayesian spatial modeling of extreme precipitation return levels, Journal of the American Statistical Association 102 (2007) 824–840. doi:10.1198/016214506000000780.

[46] D. Cooley, S. R. Sain, Spatial hierarchical modeling of precipitation extremes from a regional climate model, Journal of Agricultural, Biological, and Environmental Statistics 15 (2010) 381–402. doi:10.1007/s13253-010-0023-9.

[47] T. Gneiting, W. Kleiber, M. Schlather, Matérn Cross-Covariance Functions for Multivariate Random Fields, Journal of the American Statistical Association 105 (2010) 1167–1177. doi:10.1198/jasa.2010.tm09420.

[48] T. V. Apanasovich, M. G. Genton, Y. Sun, A Valid Matérn Class of Cross-Covariance Functions for Multivariate Random Fields With Any Number of Components, Journal of the American Statistical Association 107 (2012) 180–193. doi:10.1080/01621459.2011.643197.

[49] A. O. Finley, S. Banerjee, A. E. Gelfand, spBayes for large univariate and multivariate point-referenced spatio-temporal data models, Journal of Statistical Software 63 (2015) 1–28. doi:10.18637/jss.v063.i13.

[50] L. K. Read, R. M. Vogel, Reliability, return periods, and risk under nonstationarity, Water Resources Research 51 (2015) 6381–6398. doi:10.1002/2015WR017089.

[51] L. Cheng, A. Aghakouchak, E. Gilleland, R. W. Katz, Non-stationary extreme value analysis in a changing climate, Climate Change 127 (2014) 353–369. doi:10.1007/s10584-014-1254-5.

[52] J. D. Salas, J. Obeysekera, Revisiting the Concepts of Return Period and Risk for Nonstationary Hydrologic Extreme Events, Journal of Hydrologic Engineering 19 (2014) 554–568. doi:10.1061/(ASCE)HE.1943-5584.0000820.

[53] P. R. Sheppard, A. C. Comrie, G. D. Packin, K. Angersbach, M. K. Hughes, The climate of the US Southwest, Climate Research 21 (2002) 219–238.

[54] M. J. Menne, I. Durre, R. S. Vose, B. E. Gleason, T. G. Houston, An Overview of the Global Historical Climatology Network-Daily Database,

760 Journal of Atmospheric and Oceanic Technology 29 (2012) 897–910.
761 doi:10.1175/JTECH-D-11-00103.1.

762 [55] R. W. Higgins, Y. Chen, A. V. Douglas, Interannual Variability of
763 the North American Warm Season Precipitation Regime, Journal of
764 Climate 12 (1999) 653–680. doi:10.1175/1520-0442(1999)012<0653:
765 IVOTNA>2.0.CO;2.

766 [56] A. Mamalakis, J. Y. Yu, J. T. Randerson, A. Aghakouchak, E. Foufoula-
767 Georgiou, A new interhemispheric teleconnection increases predictabil-
768 ity of winter precipitation in southwestern US, Nature Communications
769 9 (2018) 1–10. doi:10.1038/s41467-018-04722-7.

770 [57] G. J. McCabe, M. A. Palecki, J. L. Betancourt, Pacific and At-
771 lantic Ocean influences on multidecadal drought frequency in the United
772 States, Proceedings of the National Academy of Sciences of the
773 United States of America 101 (2004) 4136–4141. doi:10.1073/pnas.
774 0306738101.

775 [58] K. Wolter, M. S. Timlin, Monitoring ENSO in COADS with a seasonally
776 adjusted principal component index, in: The 17th Climate Diagnostics,
777 Norman, OK, 1993.

778 [59] K. Wolter, M. S. Timlin, Measuring the strength of ENSO events:
779 How does 1997/98 rank?, Weather 53 (1998) 315–324. doi:10.1002/
780 j.1477-8696.1998.tb06408.x.

781 [60] K. Wolter, M. S. Timlin, El Niño/Southern Oscillation behaviour since
782 1871 as diagnosed in an extended multivariate ENSO index (MEI.ext),

International Journal of Climatology 31 (2011) 1074–1087. doi:10.1002/joc.2336.

[61] Y. Zhang, J. M. Wallace, D. S. Battisti, ENSO-like Interdecadal Variability: 1900–93, Jorunal of Climate 10 (1997) 1004–1020. doi:10.1175/1520-0442(1997)010<1004:ELIV>2.0.CO;2.

[62] H. Akaike, A New Look at the Statistical Model Identification, IEEE Transactions on Automatic Control 19 (1974) 716–723. doi:10.1109/TAC.1974.1100705.

[63] G. Schwarz, "Estimating the Dimension of a Model", The Annals of Statistics 6 (1978) 461 – 464. doi:10.2307/2958889.

[64] Y. Xia, K. Mitchell, M. Ek, J. Sheffield, B. Cosgrove, E. Wood, L. Luo, C. Alonge, H. Wei, J. Meng, B. Livneh, D. Lettenmaier, V. Koren, Q. Duan, K. Mo, Y. Fan, D. Mocko, Continental-scale water and energy flux analysis and validation for the North American Land Data Assimilation System project phase 2 (NLDAS-2): 1. Intercomparison and application of model products, Journal of Geophysical Research: Atmospheres 117 (2012). doi:10.1029/2011JD016048.

[65] S. Banerjee, B. P. Cariln, A. E. Gelfand, Modeling and Analysis for Spatial Data, CRC Press, Boca Raton, 2004.

[66] N. A. C. Cressie, Statistics for Spatial Data, volume 15 of *Wiley Series in Probability and Statistics*, John Wiley & Sons, Inc., Hoboken, NJ, USA, 1993. doi:10.1002/9781119115151.

[67] E. Gilleland, R. W. Katz, ExtRemes 2.0: An extreme value analysis package in R, Journal of Statistical Software 72 (2016) 1–39. doi:10.18637/jss.v072.i08.

[68] C. P. Robert, G. Casella, Monte Carlo Statistical Methods, Springer Texts in Statistics, Springer, New York, NY, 2004. doi:10.1007/978-1-4757-4145-2.

[69] A. W. Bowman, A. Azzalini, Applied smoothing techniques for data analysis : the kernel approach with S-Plus illustrations, Clarendon Press, 1997.

[70] J. M. Ver Hoef, N. Cressie, Multivariable spatial prediction, Mathematical Geology 25 (1993) 219–240. doi:10.1007/BF00893273.

[71] R Core Team, R: A Language and Environment for Statistical Computing, R Foundation for Statistical Computing, Vienna, Austria, 2017.

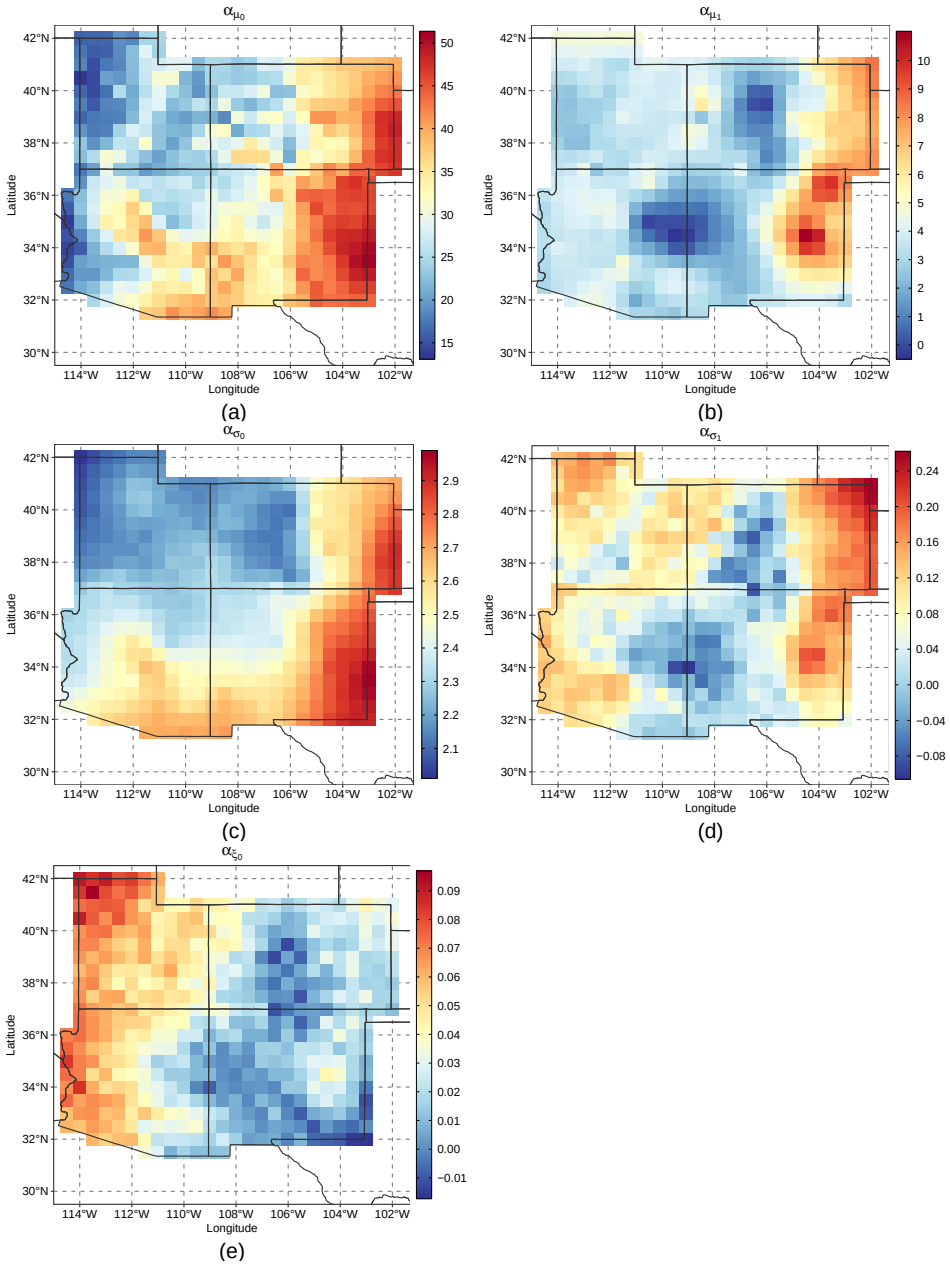

Figure 6: The conditional posterior median of the regression coefficients of GEV parameters over a 0.5-degree grid: (a) intercept of the location parameter, $\boldsymbol{\alpha}_{\mu_0}$; (b) SASP coefficient of the location parameter, $\boldsymbol{\alpha}_{\mu_1}$; (c) intercept of the log of the scale parameter, $\boldsymbol{\alpha}_{\sigma_0}$; (d) SASP coefficient of the log of the scale parameter, $\boldsymbol{\alpha}_{\sigma_1}$; and (f) shape parameter, $\boldsymbol{\alpha}_{\xi_0}$.

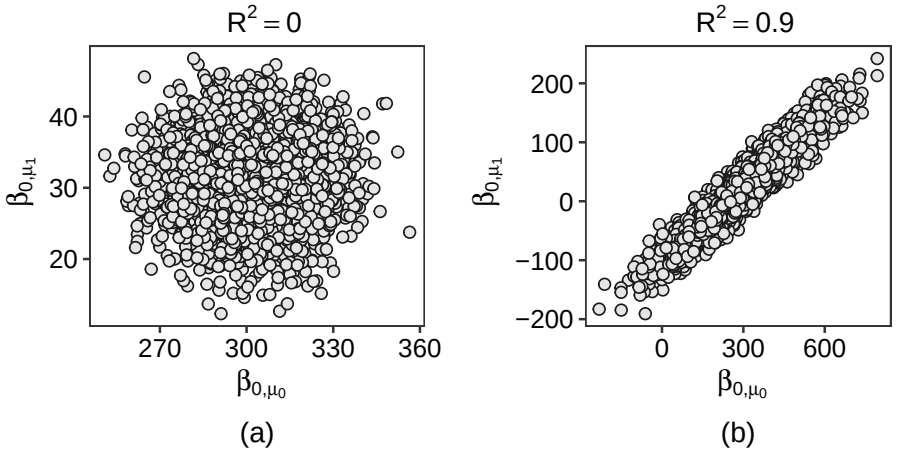

Figure 7: Scatter plots of the conditional posterior spatial regression coefficients intercept of μ_1 vs. intercept of μ_0 for: (a) semi-Bayesian univariate model; (b) semi-Bayesian multivariate model. Correlation coefficient for the semi-Bayesian multivariate model is significant at a significance level of 0.01.

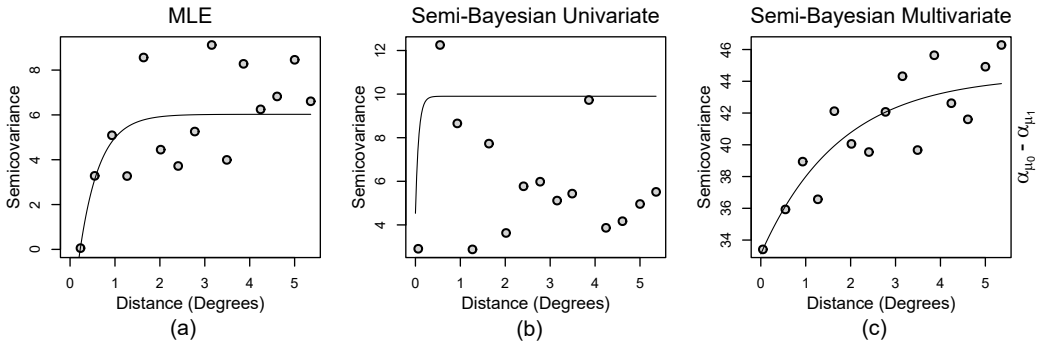

Figure 8: Sample cross-variograms of $\boldsymbol{\alpha}_{\mu_0}$-$\boldsymbol{\alpha}_{\mu_1}$ from: (a) the predicted residuals obtained from the linear model fitting on the maximum likelihood estimates of the GEV regression coefficients; (b) the conditional posterior residuals obtained from the semi-Bayesian univariate model; (c) the posterior residuals obtained from the semi-Bayesian multivariate model. Solid lines represent the least squares estimation of the exponential model of the cross-variogram.

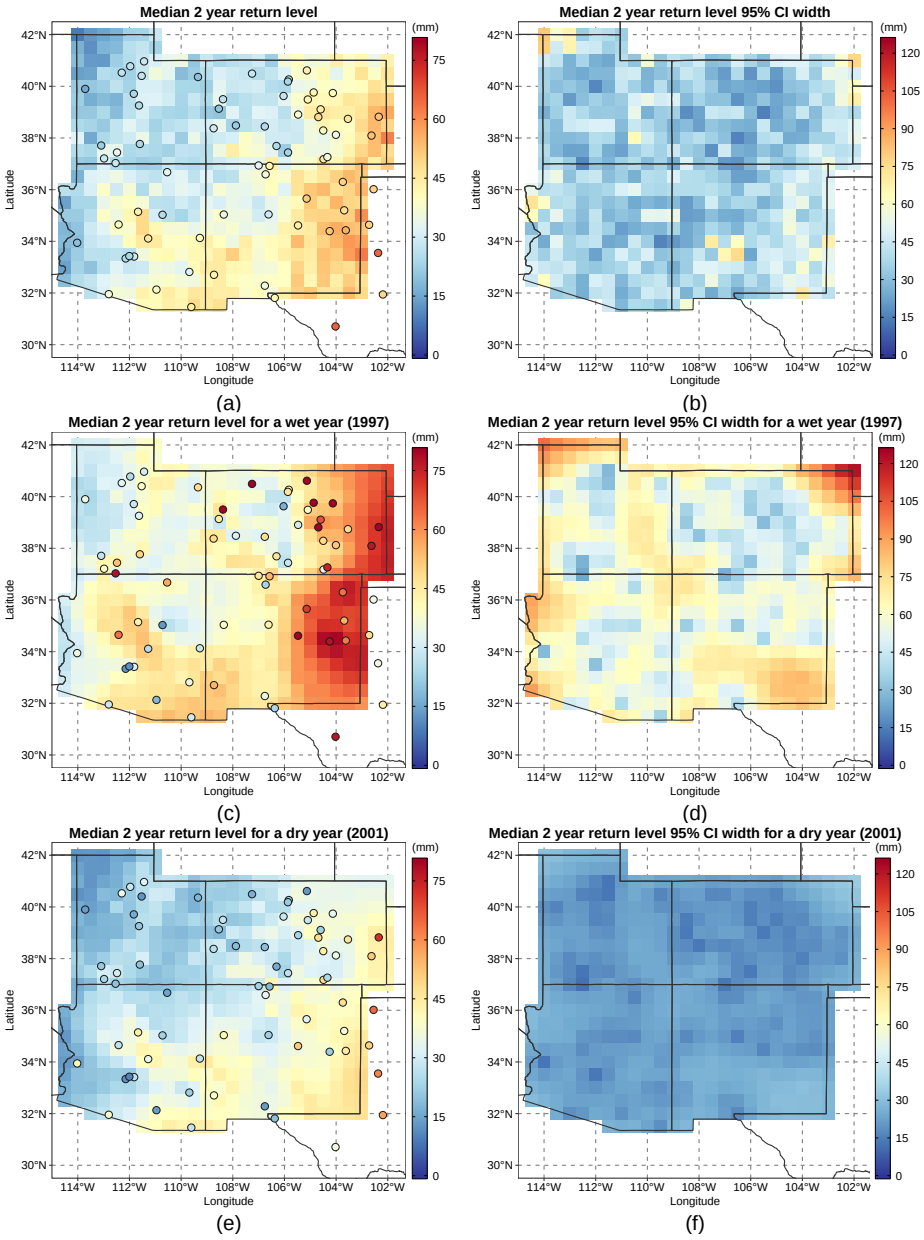

Figure 9: Conditional posterior median 2-year return level of extreme summer precipitation and median 2-year return level of 95% confidence interval width of extreme summer precipitation for the whole record (a and b), a wet year (1997, c and d), a dry year (2001, e and f). Points correspond to the median of the observed for the whole record, and the observed for wet and dry years.

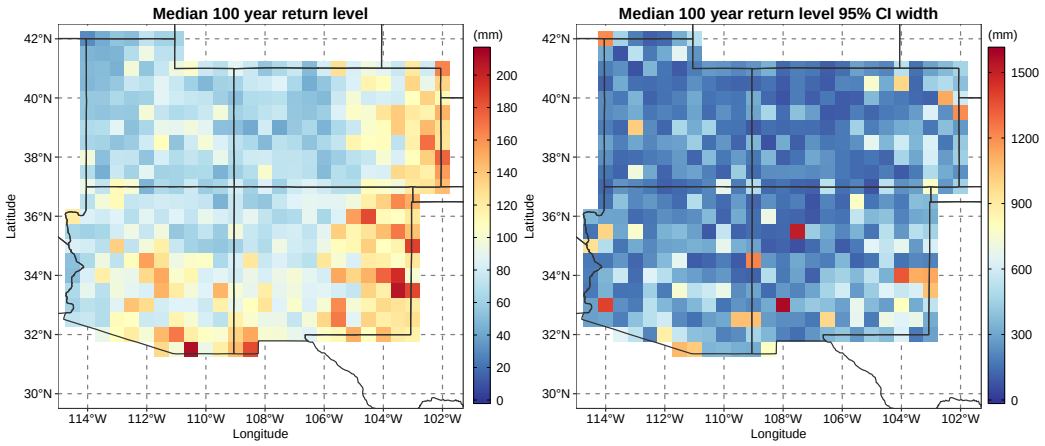

Figure 10: Conditional posterior median 100-year return level of extreme summer precipitation along with the median of the observed (left) and median 100-year return level of 95% confidence interval width of extreme summer precipitation (right).

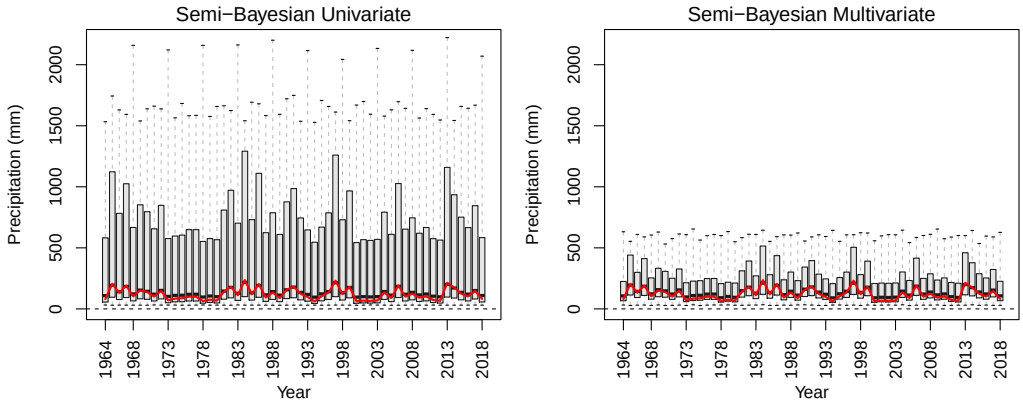

Figure 11: Nonstationary 100-year return levels from (a) the semi-Bayesian univariate model (b) the semi-Bayesian multivariate model of extreme summer precipitation at Pasamonte station, NM. Red line corresponds to the nonstationary 100-year return levels from the MLE estimates of the GEV regression coefficients.

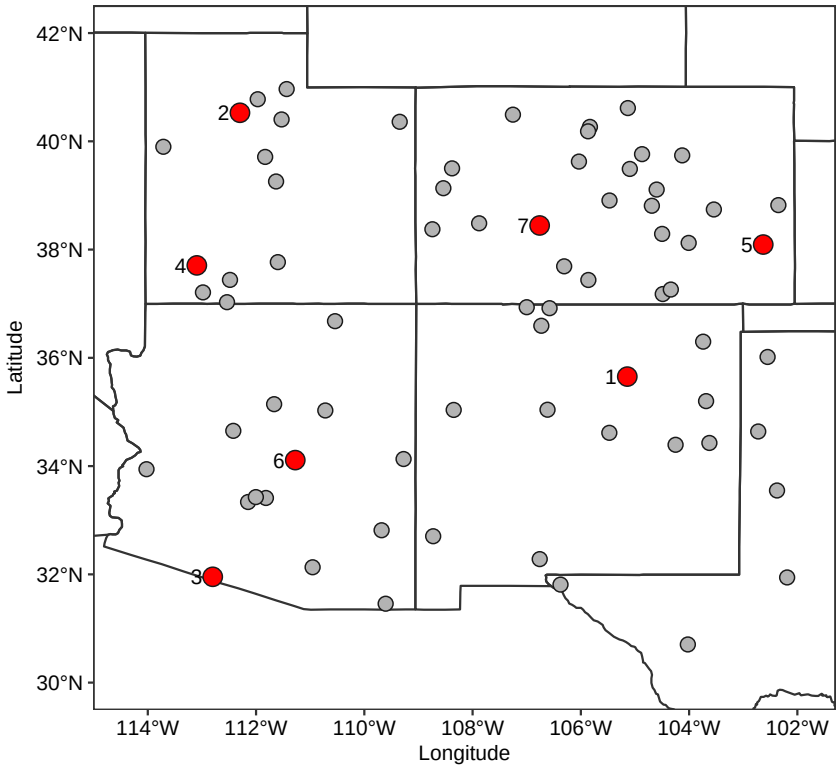

Figure 12: stations dropped (7) for the cross-validation (red circles) and the subset data (66 stations) using to fit the model (gray circles).

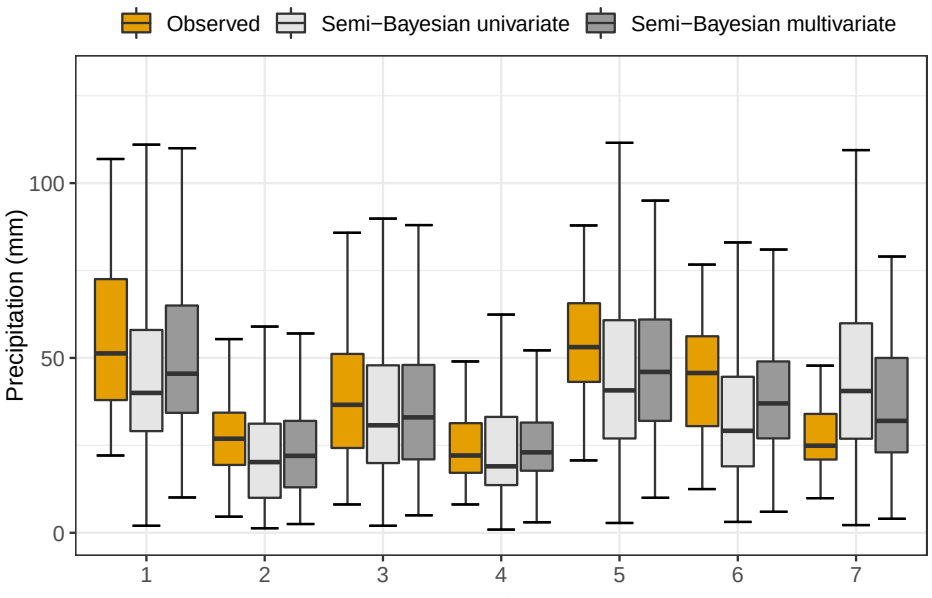

Figure 13: Predicted extreme summer precipitation (1964-2018) at 10% random leave-out stations for the validation model dropping 10% of the data for the semi-Bayesian univariate model (light gray boxes), semi-Bayesian multivariate model (gray boxes), and observed data (yellow boxes). The whiskers show the 95% credible intervals, the boxes the interquartile range, and the horizontal lines inside the boxes, the median.

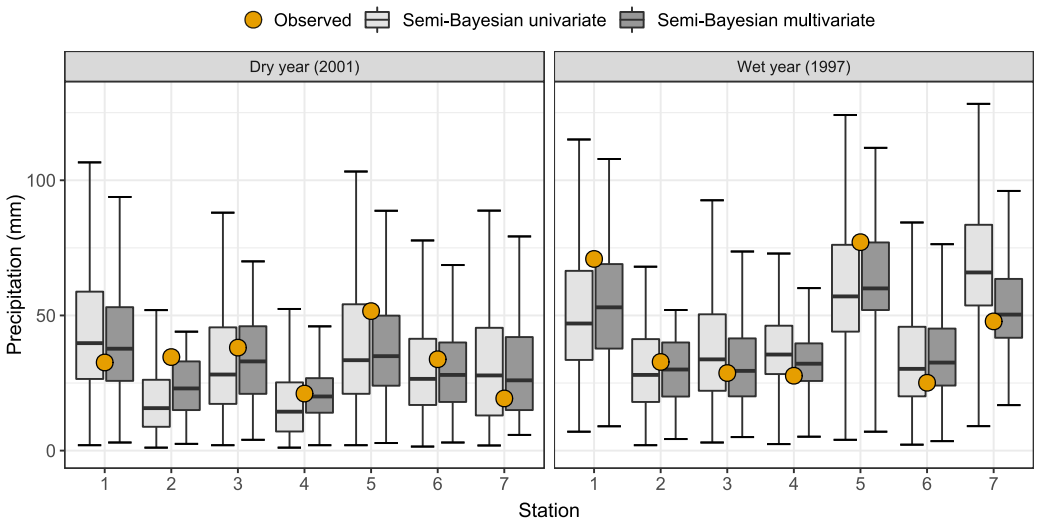

Figure 14: Predicted extreme summer precipitation for a dry (2001, left) and a wet (1997, right) year at 10% random leave-out stations for the validation model dropping 10% of the data for the semi-Bayesian univariate model (light gray boxes), semi-Bayesian multivariate model (gray boxes), and the observed data (yellow circles). The whiskers show the 95% credible intervals, the boxes the interquartile range, and the horizontal lines inside the boxes, the median.

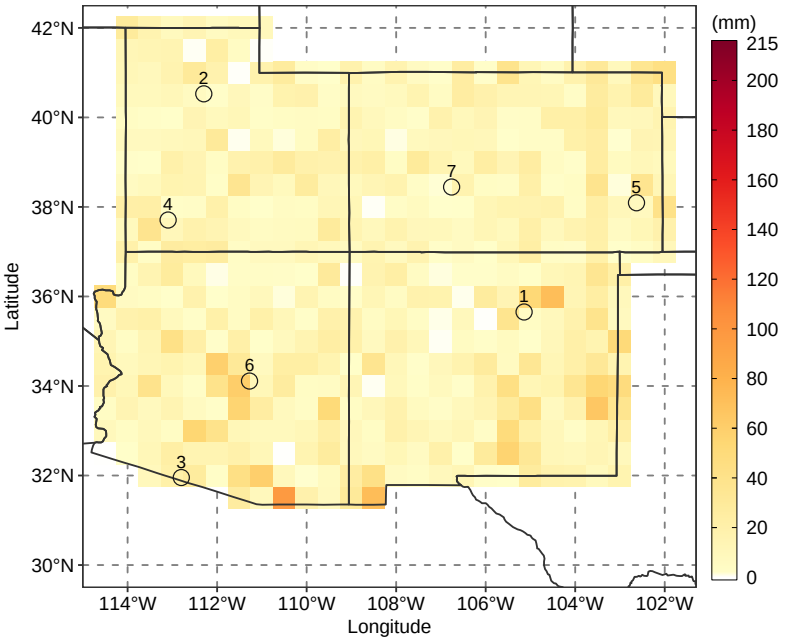

Figure 15: Difference between median return levels from the full model and the validation model dropping 10% of the data over the 0.5-degree grid. Circles correspond to the stations dropped (7) for the cross-validation. Note the scale keeps the upper limit of the median 100-year return level of extreme summer precipitation (Figure 10).